

Disjoining Pressure of Water in Nanochannels

*An Zou, Sajag Poudel, and Shalabh C. Maroo**

Department of Mechanical and Aerospace Engineering, Syracuse University, Syracuse, NY 13244

*corresponding author: scmaroo@syr.edu

Abstract: Experiments of water wicking in 1D silicon-dioxide nanochannels of heights 59 nm, 87 nm, 124 nm and 1015 nm are used to estimate the disjoining pressure of water which was found to be as high as ~ 1.5 MPa while exponentially decreasing with increasing channel height. Such a relation resulting from curve fitting of experimentally-derived data was implemented and validated in computational fluid dynamics. This methodology integrates experimental nanoscale physics into continuum simulations thus enabling the numerical study of various phenomena where disjoining pressure plays an important role.

Main Text

A nanoscale thin liquid film on a surface can have significantly different properties than its bulk form [1]. At such short distances, intermolecular interactions with surface atoms can dominate and define new equilibrium positions/velocities of liquid atoms; as these fundamental parameters are statistically averaged to estimate thermodynamic properties [2], substantial changes in density, pressure, surface tension, viscosity, etc. can occur. Distances at which a surface can affect liquid properties depends on the atomic composition: if either atom is non-polar, the presence of only weak and short-range van der Waal's force limits such changes to < 5 nm [3,4]; however, if both atoms are polar, strong and long-range electrostatic forces can alter properties up to tens to hundreds of nanometers from the surface [5-7]. The latter scenario often occurs in practical situations involving water on various surfaces.

In this work, we focus on the pressure of nanoscale water films. The pressure in such thin films is expected to be reduced based on the modified Young-Laplace equation [8]. Such a reduction, defined as disjoining pressure [9], plays a fundamental role in a wide range of engineering and natural systems involving bubbles [8,10-14], transpiration [15,16], emulsions [17-21], and membranes [22]. Theoretical determination of disjoining pressure of water on surfaces using DLVO theory requires fitted constants [20] while numerical simulations such as molecular dynamics are currently inept to computationally simulate large domains while accurately capturing the intermolecular forces of water. Likewise, the experimental estimation of sub-100 nm liquid films has been severely limited to non-polar films on solid surfaces [23,24] primarily due to the evaporative and fluidic nature of nanoscale water films. Here, we overcome these experimental challenges by characterizing water's wicking behavior in 1D silicon-dioxide (SiO_2) nanochannels of varying height, estimating the disjoining pressure of water from experimental data, and applying these disjoining pressure values in computational fluid dynamics (CFD) wicking simulations.

Figure 1a shows the sketch of a typical sample used in our experiments. The nanochannels are ~ 2 cm long and $10 \mu\text{m}$ wide, with a $10 \mu\text{m}$ spacing between two adjacent channels (please refer to supplementary for sample fabrication). We fabricated four channel heights of 59, 87, 124, and 1015 nm (Fig. 1b). A $\sim 50 \mu\text{m}$ deep reservoir was etched at each end of the channels. To conduct experiments, a DI water drop was placed in one reservoir causing the water to wick into the nanochannels and reach the other end. The top view of this wicking process was recorded using a high speed camera, where a wicking distance l was defined as the distance between the entrance and the position of the meniscus at a given time t (Fig. 1c). A microscope with a $50\times$ objective was optionally connected to the camera to obtain a close-up view of the meniscus during wicking. After the experiment, the sample was dried by heating it to $\sim 200^\circ\text{C}$ on a hot plate in open air with the drying time ranging from several minutes up to several hours depending on the nanochannel height. Wicking experiments for each channel height were conducted at least four times to ensure repeatability.

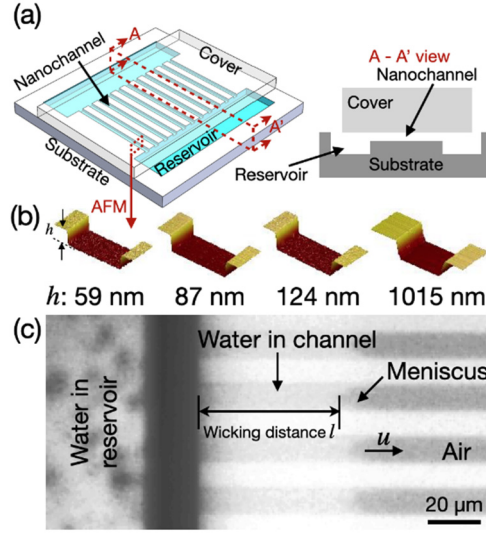


Figure 1: (a) Sketch of the sample with nanochannels and reservoirs for wicking experiments. (b) Atomic force microscope (AFM) images of the fabricated nanochannels of different heights. (c) Optical microscope image of water wicking into nanochannels of height 59 nm; the black dots in reservoir are roughness introduced from deep silicon etching during sample fabrication while the black bar at the entrance is the edge of the reservoir which is out of focus.

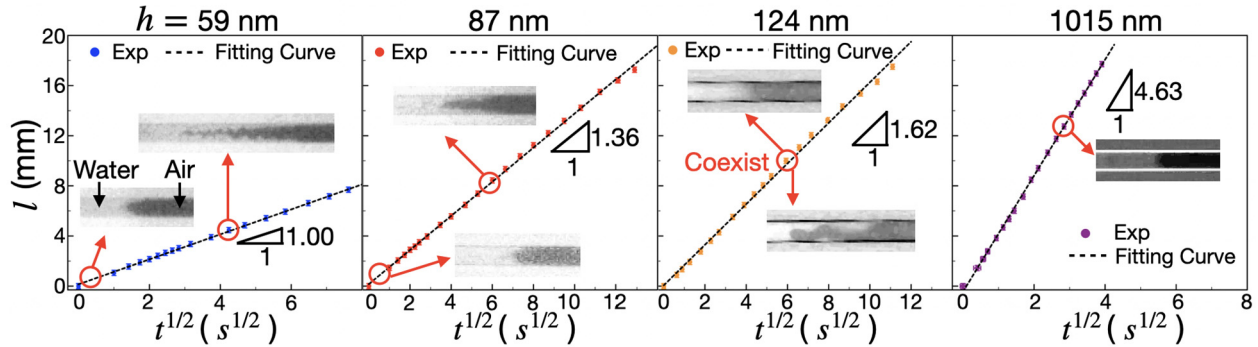


Figure 2: Variation of wicking distance l with $t^{1/2}$ in 59 nm, 87 nm, 124 nm, and 1015 nm channels. The insets are top-view images from optical microscope showing the two different meniscus shapes observed in the experiments.

The wicking distance l variation with time t is plotted in Fig. 2; l is found to be proportional to $t^{1/2}$ for all channel heights as predicted by the analytical solution of Navier-Stokes equation for a high aspect ratio (height \ll width) rectangular cross-section channel [25]:

$$l = \sqrt{\frac{h^2 [1 - 0.63(\frac{h}{w})] \Sigma P}{6\mu}} \cdot t^{1/2} \approx \sqrt{\frac{h^2 \Sigma P}{6\mu}} \cdot t^{1/2} = C \cdot t^{1/2} \quad (1)$$

where h and w are height and width of the nanochannel, respectively; μ is the fluid dynamic viscosity; and ΣP is the total pressure difference driving the wicking. The value of constant C (i.e. the slope in Fig. 2) is obtained from the linear curve fitting of experimental data in Fig. 2 for the highest R^2 value, and it increases with increasing channel height as expected. During the wicking process, two types of meniscus were observed: regular-curved shape and wedge shape (insets in Fig. 2). In 1015 nm channel height, the meniscus

was always of regular-curved shape as it moved in the entire channel length (~ 2 cm). However, in 59 nm and 87 nm height channels, the regular-curved meniscus occurred only within the first few hundreds of microns from the entrance. Beyond this initial distance, water was seen to flow faster at the corners forming the wedge-shape meniscus, which also led to air or vapor being momentarily trapped within the wicking liquid front [26]. Meanwhile, the 124 nm height channel was transitional as both types of meniscus simultaneously co-existed in neighboring channels even at lengths far away from entrance (~ 1.5 cm).

The most common mechanism of wicking in nanochannels is attributed to capillary pressure [27]. If wicking is only driven by capillary pressure (i.e. $\Sigma P = P_c \approx 2\sigma \cos\theta/h$) where σ is the surface tension, and θ is the contact angle, Eq. 1 can be simplified to the widely-used Washburn equation for capillary filling [28]:

$$l = \sqrt{\frac{\sigma h \cos\theta}{3\mu}} \cdot t^{1/2} \quad (2)$$

Although the linear dependence of wicking distance on $t^{1/2}$ holds at nanoscale, Washburn equation is inconsistent in predicting the experimental wicking rate. Other published literature on wicking in rectangular cross-section nanochannels have found a similar observation [26,29-32] and explained this inconsistency primarily due to electroviscous effect [32-36] or geometrical effect [37,38]. However, these effects do not explain our observed deviation (please refer to supplementary for detailed explanation). Further, a common major flaw in these prior studies is the contact angle θ used in Eq. 2. We should not inherently assume a uniform contact angle [26,32,39,40] of the meniscus due to the channel's high aspect ratio (width is ~ 10 μm for all channels while height varies from 0.059 μm to 1.015 μm). Thus, due to the rectangular cross-section of the channel, we define two separate contact angles θ_{top} and θ_{side} of the meniscus corresponding to the top and side views, respectively (Fig. 3a).

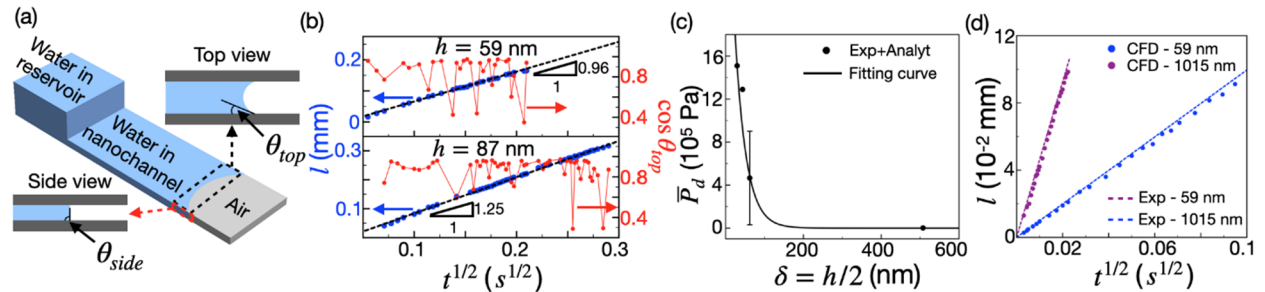


Figure 3: (a) Sketch showing the difference in contact angles from top and side views. (b) Measured wicking distance and $\cos \theta_{top}$ as a function of $t^{1/2}$ in 59 nm and 87 nm channels during the initial time when the meniscus was only regular-curve shaped; (c) Estimated average disjoining pressure \bar{P}_d of water in silicon-dioxide nanochannels for various water film thickness δ based on nanochannel height h , and the corresponding exponentially fitted curve with $R^2 = 0.97$. (d) Comparison of experimental wicking rate with that from CFD simulations where average disjoining pressure data of (c) is integrated into the simulations.

Figure 3b plots the change in θ_{top} for the 59 nm and 87 nm channel heights along with their respective wicking rates during the initial time period when the meniscus is regular-curved shape (please see supplementary for θ_{top} estimation from optical microscope images). The experimental data presents two unique findings: (1) despite as much as 50% fluctuation in the values of $\cos \theta_{top}$, the wicking distance l is still proportional to $t^{1/2}$ (Fig. 3b), and (2) the fitting curve slopes of 0.96 and 1.25 $\text{mm/s}^{1/2}$ for 59 nm and 87 nm channels, respectively, during the initial wicking period (Fig. 3b) are in good agreement with the values for the entire wicking period (1.00 and 1.36 $\text{mm/s}^{1/2}$ respectively in Fig. 2) even though the meniscus shape drastically changes from regular-curved shape to wedge-shape. These observations imply that capillary

pressure, which is strongly dependent on meniscus shape, does not govern the wicking phenomenon in smaller channel heights of 59 nm and 87 nm. Instead, disjoining pressure must be the driving force as most or all of the water in these nanochannels interact with the solid surface owing to the small height. The opposite holds true for the larger channel height of 1015 nm where only the steady regular-curved shape meniscus occurs implying that capillary pressure drives wicking, as merely a small fraction of the total water is affected by the surface. In the transitional 124 nm height channel, both disjoining and capillary pressures are important. The importance of both pressures at this channel height also alludes to the idea that the effect of SiO₂ surface on water (i.e. disjoining pressure) starts to significantly diminish at distances beyond $h/2 \sim 60$ nm from the surface, and is in good agreement with published studies [6,7] which found the distance to be ~ 50 nm using nuclear magnetic resonance. Next, we use the experimental data to calculate disjoining pressure in the nanochannels.

Disjoining pressure is theoretically known to continuously decrease with increasing distance from the surface [41]. However, as we only have four channel heights, disjoining pressure \bar{P}_d averaged over half the channel height is estimated from experimental data using Eq. 1 and $\Sigma P = \bar{P}_d + P_c$, the combination of which can be rearranged into:

$$\bar{P}_d = \Sigma P - P_c = \frac{6\mu C^2}{h^2} - 2\sigma \left(\frac{\cos\theta_{side}}{h} + \frac{\cos\theta_{top}}{w} \right) \quad (3)$$

where C is the slope (from Fig. 2) of the wicking rate and θ_{top} is obtained from top view images as mentioned earlier. It should be noted here that although properties of water (μ and σ) in such confined channels will be different from the bulk, we still assume bulk properties as per the norm in literature [30-34,37] and also due to the fact that such properties have not yet been directly measured in experiments; in fact, disjoining pressure term is introduced in the modified Young-Laplace equation [10,23] to account for the lack of such properties at these scales. Thus, in Eq. 3, all parameters are known except θ_{side} . However, as the heights of the channels are at nanoscale, it is not possible to experimentally measure θ_{side} . Considering the published experimental finding that water molecules on a glass surface are highly ordered upto distances of 50 nm perpendicular to the surface [6,7] (i.e. channel heights of upto 100 nm in our case), we use molecular dynamics simulations to qualitatively study the effect of liquid structuring on contact angle by simulating wicking of liquid argon in a hydrophilic nanochannel of two different heights (please see supplementary for simulation details and results). For the smaller channel height where liquid structuring is prominent, θ_{side} is obtained to be $\sim 90^\circ$, whereas the larger channel height with mostly bulk liquid resulted in θ_{side} of $\sim 45^\circ$. Thus, using the same analogy for water in our SiO₂ nanochannels, we assume θ_{side} as 90° for the smaller height channels (59 nm and 87 nm) and $\theta_{side} = \theta_{top} = 39.6^\circ$ for larger channel height (1015 nm) in Eq. 3 to estimate \bar{P}_d (Fig. 3c). For the transitional channel with the height of 124 nm, θ_{side} would be between 90° and θ_{top} ; hence, we take the average of upper and lower \bar{P}_d values based on this range of θ_{side} while simultaneously showing the limits (Fig. 3c). Please see supplementary for the values of \bar{P}_d and P_c for each channel height. Thus, \bar{P}_d of water in silicon-dioxide nanochannels is found to exponentially decrease with increasing water film thickness δ (Fig. 3c) which is equivalent to half the channel height $h/2$. We choose the exponential relation as polar molecules exhibit dominant electrostatic interaction as compared to power law function when only van der Waals interaction is present [20]. Such a relation can be expressed as:

$$\bar{P}_d = A \cdot e^{-b\delta} \quad (4)$$

where $A = 4.25 \times 10^6$ Pa, and $b = 0.035 \text{ nm}^{-1}$. The values of constants A and b are obtained from curve fitting the experimental data of Fig. 3c.

Lastly, we implement Eq. 4 in commercial CFD software ANSYS Fluent [42] to show the applicability of experimentally derived \bar{P}_d values into continuum simulations. Similar to the experiments,

we simulate wicking of water in 59 nm and 1015 nm channels (please see supplementary for details) using a laminar multiphase volume of fluids (VOF) method [43]. As the driving force of the wicking is $\Sigma P = \bar{P}_d + P_c$, P_c is achieved through continuous surface force (CSF) modeling [44] along with wall adhesion and \bar{P}_d is invoked by a user-defined-function (udf). The different θ_{top} and θ_{side} in 59 nm channel are implemented by assigning the corresponding contact angles to side walls and top/bottom walls of the channel. Wicking rates are found to be in good agreement with experimental data in both channels (Fig. 3d) demonstrating successful implementation of disjoining pressure model in CFD. Such an integration captures nanoscale physics in continuum simulations while including the effects of disjoining pressure in various phenomena such as phase change, transpiration, etc.

To summarize, we report a fundamental study of estimating disjoining pressure of water in silicon-dioxide nanochannels through experiments of wicking in channels of heights 59 nm, 87 nm, 124 nm and 1015 nm. Disjoining pressure is found to be the primary driving force of wicking in smaller height nanochannels while capillary pressure dictates wicking in larger nanochannel height. The average disjoining pressure of water exponentially declined with increasing distance from the surface, and a relation is derived by curve fitting the experimental data. The disjoining pressure variation is implemented in CFD simulations and is shown to capture the experimental wicking behavior, thus enabling numerical study of various phenomena where disjoining pressure plays an important role.

Acknowledgements

This material is based upon work supported by, or in part by, the Office of Naval Research under contract/grant no. N000141812357. This work was performed in part at the Cornell NanoScale Facility, an NNCI member supported by NSF Grant NNCI-2025233.

Reference

- [1] W. H. Thompson, *J Chem Phys* **149** (2018).
- [2] M. P. Allen and D. J. Tildesley, *Computer simulation of liquids* (2017).
- [3] H. Hu, C. R. Weinberger, and Y. Sun, *Nano Lett* **14**, 7131 (2014).
- [4] Y. D. Sumith and S. C. Maroo, *J Phys Chem Lett* **6**, 3765 (2015).
- [5] R. Mancinelli, S. Imberti, A. K. Soper, K. H. Liu, C. Y. Mou, F. Bruni, and M. A. Ricci, *J Phys Chem B* **113**, 16169 (2009).
- [6] T. Tsukahara, W. Mizutani, K. Mawatari, and T. Kitamori, *J Phys Chem B* **113**, 10808 (2009).
- [7] T. Tsukahara, A. Hibara, Y. Ikeda, and T. Kitamori, *Angew Chem Int Edit* **46**, 1180 (2007).
- [8] A. Chatterjee, J. L. Plawsky, and P. C. Wayner, *Adv Colloid Interfac* **168**, 40 (2011).
- [9] B. V. Derjaguin and N. V. Churaev, *Journal of Colloid and Interface Science* **66**, 389 (1978).
- [10] S. S. Panchamgam, A. Chatterjee, J. L. Plawsky, and P. C. Wayner, *International Journal of Heat and Mass Transfer* **51**, 5368 (2008).
- [11] A. Zou, A. Chanana, A. Agrawal, P. C. Wayner Jr, and S. C. Maroo, *Scientific Reports* **6**, 20240 (2016).
- [12] A. Zou, M. Gupta, and S. C. Maroo, *The Journal of Physical Chemistry Letters* **9**, 3863 (2018).
- [13] G. Son, V. K. Dhir, and N. Ramanujapu, *Journal of Heat Transfer* **121**, 623 (1999).
- [14] P. C. Wayner Jr., *AIChE Journal* **45**, 2055 (1999).

- [15] G. W. Koch, S. C. Sillett, G. M. Jennings, and S. D. Davis, *Nature* **428**, 851 (2004).
- [16] A. Zou, M. Gupta, and S. C. Maroo, *The Journal of Physical Chemistry Letters* **11**, 3637 (2020).
- [17] C. Stubenrauch and R. von Klitzing, *J Phys-Condens Mat* **15**, R1197 (2003).
- [18] S. D. Taylor, J. Czarnecki, and J. Masliyah, *Journal of Colloid and Interface Science* **252**, 149 (2002).
- [19] B. P. Binks, W. G. Cho, and P. D. I. Fletcher, *Langmuir* **13**, 7180 (1997).
- [20] R. H. Yoon and B. S. Aksoy, *Journal of Colloid and Interface Science* **211**, 1 (1999).
- [21] T. D. Dimitrova, F. Leal-Calderon, T. D. Gurkov, and B. Campbell, *Langmuir* **17**, 8069 (2001).
- [22] D. Exerowa, D. Kashchiev, and D. Platikanov, *Adv Colloid Interfac* **40**, 201 (1992).
- [23] S. S. Panchangam, J. L. Plawsky, and P. C. Wayner, *J Heat Trans-T Asme* **129**, 1476 (2007).
- [24] S. Dasgupta, J. L. Plawsky, and P. C. Wayner Jr, *AIChE Journal* **41**, 2140 (1995).
- [25] B. E. Rapp, in *Microfluidics: Modelling, Mechanics and Mathematics*, edited by B. E. Rapp (Elsevier, Oxford, 2017), pp. 351.
- [26] M. Yang, B. Y. Cao, W. Wang, H. M. Yun, and B. M. Chen, *Chem Phys Lett* **662**, 137 (2016).
- [27] J. W. van Honschoten, N. Brunets, and N. R. Tas, *Chem Soc Rev* **39**, 1096 (2010).
- [28] E. W. Washburn, *Phys Rev* **17**, 273 (1921).
- [29] V. N. Phan, P. Joseph, L. Djeghlaf, A. E. D. Allouch, D. Bourrier, P. Abgrall, A.-M. Gué, C. Yang, and N.-T. Nguyen, *Heat Transfer Engineering* **32**, 624 (2011).
- [30] N. R. Tas, J. Haneveld, H. V. Jansen, M. Elwenspoek, and A. van den Berg, *Appl Phys Lett* **85**, 3274 (2004).
- [31] J. Haneveld, N. R. Tas, N. Brunets, H. V. Jansen, and M. Elwenspoek, *J Appl Phys* **104** (2008).
- [32] S. Mozaffari, P. Tchoukova, A. Mozaffari, J. Atias, J. Czarnecki, and N. Nazemifard, *Colloid Surface A* **513**, 178 (2017).
- [33] V. N. Phan, C. Yang, and N. T. Nguyen, *Icnmm 2009, Pts a-B*, 907 (2009).
- [34] V. N. Phan, C. Yang, and N. T. Nguyen, *Microfluid Nanofluid* **7**, 519 (2009).
- [35] C. L. Ren and D. Q. Li, *Anal Chim Acta* **531**, 15 (2005).
- [36] C. Yang and D. Q. Li, *Journal of Colloid and Interface Science* **194**, 95 (1997).
- [37] N. R. Tas, P. Mela, T. Kramer, J. W. Berenschot, and A. van den Berg, *Nano Lett* **3**, 1537 (2003).
- [38] N. R. Tas, M. Escalante, J. W. van Honschoten, H. V. Jansen, and M. Elwenspoek, *Langmuir* **26**, 1473 (2010).
- [39] Z. R. Ye, S. B. Li, C. Wang, R. Shen, and W. J. Wen, *Rsc Adv* **6**, 2774 (2016).
- [40] A. Han, G. Mondin, N. G. Hegelbach, N. F. de Rooij, and U. Staufer, *Journal of Colloid and Interface Science* **293**, 151 (2006).
- [41] V. P. Carey and A. P. Wemhoff, *J Heat Trans-T Asme* **128**, 1276 (2006).
- [42] A. Fluent, *Academic Research. Release* **14** (2015).
- [43] C. W. Hirt and B. D. Nichols, *J Comput Phys* **39**, 201 (1981).
- [44] J. U. Brackbill, D. B. Kothe, and C. Zemach, *J Comput Phys* **100**, 335 (1992).